Optimal Design of Wire-and-Arc Additively Manufactured I-Beams for Prescribed Deflection

Matteo BRUGGI[1]*, Vittoria LAGHI[2], Tomaso TROMBETTI[2]

[1] *Department of Civil and Environmental Engineering, Politecnico di Milano, 20133, Milano, Italy*

[2] *Department of Civil, Chemical, Environmental and Materials Engineering, University of Bologna, 40136, Bologna, Italy*

* Corresponding Author e-mail: matteo.bruggi@polimi.it

Alloys fabricated by wire-and-arc additive manufacturing (WAAM) exhibit a peculiar anisotropy in their elastic response. As shown by recent numerical investigations concerning the optimal design of WAAM-produced structural components, the printing direction remarkably affects the stiffness of the optimal layouts, as well as their shape. So far, single-plate specimens have been investigated. In this contribution, the optimal design of WAAM-produced I-beams is addressed assuming that a web plate and two flat flanges are printed and subsequently welded to assemble the structural component. A formulation of displacement-constrained topology optimization is implemented to design minimum weight specimens resorting to a simplified two-dimensional model of the I-beam. Comparisons are provided addressing solutions achieved by performing topology optimization with (i) conventional isotropic stainless steel and with (ii) WAAM-produced orthotropic stainless steel at prescribed printing orientations. Lightweight solutions arise whose specific shape depends on the selected material and the adopted printing direction.

Keywords: structural optimization, topology optimization, wire-and-arc additive manufacturing, I-beams, orthotropic material, additive manufacturing, 3D printing.

1. INTRODUCTION

With the advent of the "digital turn" [1] in the early years of the 21st century new tools for free form in architecture have gained influence, enabling the design of new complex structural shapes, see e.g. [2–4]. The growth of automation and additive manufacturing (AM) technologies has prevailed in most industrial sectors, but its use in construction has been restricted to a few pioneering appli-

cations. Advantages in the digitalization of the construction sectors are foreseen in the production of more efficient structures, reduction in material waste and increase in work safety [5]. Among different AM processes, wire-and-arc additive manufacturing (WAAM) provides an opportunity to build a new generation of efficient steel structures with high geometrical flexibility and reduced material use. This metal AM process consists of off-the-shelf welding equipment mounted on top of a robotic arm, allowing for high printing speed and large-scale outcomes (up to a few meters) [6–8]. Recent studies investigated WAAM stainless steel elements from the microstructural, geometrical and mechanical point of view [9–13]. The results revealed: (i) an influence of the process parameters in both geometrical and mechanical properties [9], (ii) an influence of the geometrical irregularities (e.g., surface roughness and cross-section variation) on the mechanical response [13], and (iii) a marked mechanical anisotropy, also evidenced from the material microstructure [12, 14]. With reference to the latter, the authors calibrated from experiments a specific orthotropic elastic material model accounting for the different values of Young's modulus and Poisson's ratio with respect to the relative printing direction [15]. Very recently, anisotropic modeling was also used in the characterization of the inelastic range [16].

Topology optimization (TO) defines the material distribution making an optimal component within a design domain, based on the minimization of an objective function and a given set of constraints. Thus, it is a useful tool for designing new lightweight structural elements [17]. Given that "density" can range between 0 and 1, the solid isotropic model with penalization (SIMP) is implemented to achieve results with "voids" and "full material" [18, 19].

With the advent of AM processes, the scientific community has paid a lot of effort towards the implementation of AM and TO tools to leverage the full potential of their combined use [20, 21]. Among the others, specific features such as printing orientation (which has several mechanical implications for WAAM), manufacturing constraints and geometrical tolerances need to be properly accounted for. In many approaches of TO, printing orientation is dealt with concerning possible overhang issues, see, e.g., [22–27]. In [28], flexible fabrication beyond planar layer-by-layer deposition is explored by investigating the simultaneous design of a structure and its fabrication sequence.

In [29], a displacement-constrained minimum weight formulation was presented for WAAM plates accounting for the orthotropic material model derived in [15]. In particular, the design variables were set as both the density field and the printing direction, i.e., the angle between the symmetry axes of the orthotropic alloy and the axes of the reference system in which the part is framed. Numerical simulations were reported to show that the build orientation remarkably affects the shape and the stiffness of the optimal layouts in case of single-plate specimens.

In this work, the optimal design of WAAM-produced I-beams is addressed assuming that a web plate and two flat flanges are printed and subsequently welded to assemble the structural component. A layer-by-layer manufacturing process that adopts the same build orientation within each printed part is considered. Indeed, in the fabrication of a single part, the WAAM process usually adopts the same printing orientation to pursue high-quality outcomes [9]. Prescribed printed directions are taken into account with regard to the anisotropy affecting the mechanical response of the built material used in each plate. A formulation of displacement-constrained TO is implemented to design minimum weight specimens resorting to a simplified two-dimensional modeling of the I-beam. In [30], an integrated TO technique with concurrent use of both four-node quadrilateral finite elements and two-node beam elements was originally proposed to design structural braced frames that are part of the lateral system of a high-rise building. In the present work, two-node truss elements are combined with four-node finite elements to account for the axial forces in the flanges along with the state of orthotropic plane stress in the web of the I-beam. The arising optimization problem is written in terms of the material density in the web and the cross-sectional area of the two flanges. Sequential convex programming is adopted to solve the problem [31]. The adjoint method is exploited to compute derivatives of the objective function and constraint(s) with respect to the minimization unknowns. This may be performed in an efficient way, especially in the case of multiple sets of displacement constraints, as in the case of distributed loads.

Optimal shapes achieved by performing TO with (i) conventional isotropic stainless steel and with (ii) WAAM-produced (orthotropic) stainless steel for prescribed orientations are compared and commented on. Lightweight solutions arise whose peculiar shape strictly depends on the selected material and the adopted printing direction.

The proposed approach must be intended as a preliminary design tool to sketch shapes for lightweight I-beams. The material characterization herein presented refers to as-built plates, without any post-processing treatment. This has the goal of assessing the feature of the printed alloy in the condition in which it is likely to be used for structural engineering applications. Besides the anisotropy in the mechanical response, the WAAM process induces some non-negligible aspects. Residual stresses are crucial for WAAM-produced elements and should be considered for more sophisticated modelling. As reported e.g., in [32], the high heat input is responsible for stresses that might affect the service life and structural integrity of the printed component. For example, an overarching digital twin accounting for any process-induced effects could be developed and integrated within the optimization procedure to comprehend the generation and distribution of residual stresses and to mitigate them. Also, flexural

buckling of the web plate and lateral torsional buckling of the I-beam should be accounted for, due to the limited thickness of the printed plates. The simple optimization problem herein proposed could be suitably extended to cover these issues, by introducing a more complex modeling and relevant sets of constraints.

The paper is organized as follows. Section 2 is devoted to reviewing WAAM stainless steel with special regard to the orthotropic material model. The design of I-beams within a displacement-constrained minimum weight problem is addressed in Sec. 3. Section 4 presents numerical simulations, whereas Sec. 5 concerns conclusions and addresses the need for further research.

2. The wire-and-arc additively manufactured material

Within the AM category of directed energy deposition (DED) processes, WAAM appears to be the most suitable for realizing large-scale metal parts for structural engineering purposes [8]. It is defined as the combination of an electric arc as a heat source to melt the wire feedstock and deposit it in a layer-upon-layer fashion [7]. Thus, the printed outcome is characterized by two main directions, e.g., one along the deposited layer (longitudinal direction) and one perpendicular to it (transversal direction), see Fig. 1. Several experimental studies were carried out on WAAM-produced elements to investigate their features in terms of geometrical properties, mechanical response and microstructure [9, 10, 12, 13]. In [13], the discrepancy between the nominal geometry and the printed outcome was studied with regard to the possible influence on the mechanical response. In [12, 14], the mechanical response through tensile tests was matched with microstructural analyses to underline the anisotropic nature of WAAM stainless
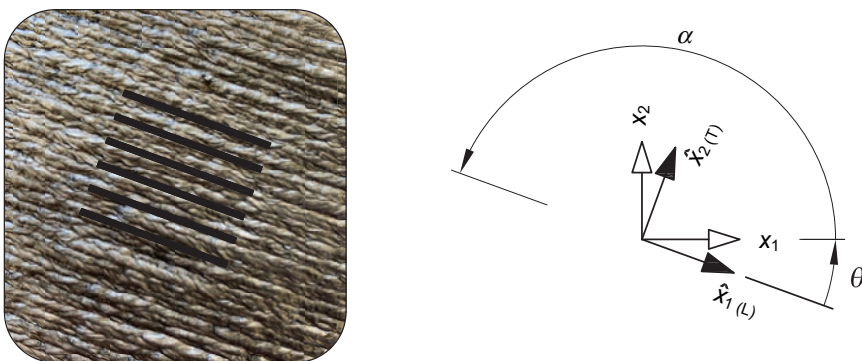

Fig. 1. Orientation of the printed layers for a WAAM-fabricated object described in the general reference system with axis x_1 and x_2. The symmetry axes of the orthotropic medium are denoted as $\hat{x}_1$ and $\hat{x}_2$: the printing direction (L) and the transversal direction (T), respectively.

steel, which affects the response of the members, so that stiffness and strength parameters depend on the relative printing direction. Wide experimental work was carried out at the University of Bologna labs to characterize WAAM stainless steel for structural engineering applications. For this aim, a series of experimental tests on planar and rod-like specimens was developed. The main results consisted in: (i) a detailed study of the inherent geometrical variability and specimen-to-specimen variability in terms of cross-section variation; (ii) the definition of three main printing directions (e.g., transversal, T, longitudinal, L, and diagonal, D, at 45° from the previous ones) to evaluate the mechanical response of planar elements; (iii) the estimation of the different mechanical response under tensile loading of specimens left as-printed (e.g., with a rough surface) and milled before the test [12, 13, 33]. The tests confirmed a remarkable influence on the relative printing orientation arising for stiffness parameters [15].

2.1. Orthotropic plane stress modeling

The material symmetries of the plates fabricated through the WAAM process require the adoption of an orthotropic plane stress material model. The symmetry axes of the orthotropic material are denoted as $\widehat{x}_1$ and $\widehat{x}_2$, i.e. the printing direction (L) and the transversal direction (T), respectively, see Fig. 1. Kelvin's notation is used in the derivation that follows because of its algebraic properties, see in particular [34] and [35].

In the material reference system $O\widehat{x}_1\widehat{x}_2$, the components of the stress tensor are re-gathered in the array $\widehat{\boldsymbol{\sigma}} = [\widehat{\sigma}_{11} \quad \widehat{\sigma}_{22} \quad \sqrt{2}\widehat{\sigma}_{12}]^T$ and, equally, $\widehat{\boldsymbol{\varepsilon}} = [\widehat{\varepsilon}_{11} \quad \widehat{\varepsilon}_{22} \quad \sqrt{2}\widehat{\varepsilon}_{12}]^T$ for the components of the strain tensor. Hence, the compliance matrix of the stress-strain relation $\widehat{\boldsymbol{\varepsilon}} = \widehat{\mathbf{S}}_0 \, \widehat{\boldsymbol{\sigma}}$ reads:

$$\widehat{\mathbf{S}}_0 = \begin{bmatrix} \dfrac{1}{\widehat{E}_1} & -\dfrac{\widehat{\nu}_{21}}{\widehat{E}_2} & 0 \\[3mm] -\dfrac{\widehat{\nu}_{12}}{\widehat{E}_1} & \dfrac{1}{\widehat{E}_2} & 0 \\[3mm] 0 & 0 & \dfrac{1}{2\widehat{G}_{12}} \end{bmatrix}, \tag{1}$$

where $\widehat{E}_1$, $\widehat{E}_2$ are Young's moduli of the material along $\widehat{x}_1$ and $\widehat{x}_2$, respectively, $\widehat{\nu}_{12}$, $\widehat{\nu}_{21}$ are Poisson's ratios ($\widehat{\nu}_{ij} > 0$ corresponds to a contraction in direction $\widehat{x}_j$ when an extension is applied in direction $\widehat{x}_i$) and $\widehat{G}_{12}$ is the in-plane shear modulus. It is worth recalling that the equality $\widehat{\nu}_{12}\widehat{E}_2 = \widehat{\nu}_{21}\widehat{E}_1$ holds.

Following [15] and [29], Young's moduli along $\widehat{x}_1$ and $\widehat{x}_2$ may be assumed equal to the relevant mean values derived from the experimental tests, i.e.,

$\widehat{E}_1 = E_L = 135.84$ GPa and $\widehat{E}_2 = E_T = 106.09$ GPa. To preserve the symmetry of $\widehat{\mathbf{S}}_0$, a minimization problem must be formulated to process the mean values of the Poisson's ratios read in the longitudinal and in the transversal direction, ν_{LT} and ν_{TL}, respectively, deriving $\widehat{\nu}_{12} = 0.47$ and $\widehat{\nu}_{12} = 0.37$. The shear modulus $\widehat{G}_{12} = 151.25$ GPa may be derived using the mean value of the apparent Young's modulus in the diagonal direction $E_D = 243.09$ GPa, which is known from experimental investigations.

A general reference system Ox_1x_2 is defined, denoting by θ the counterclockwise rotation of the axis x_1 with respect to $\widehat{x}_1$. Assuming that the design domain is described in Ox_1x_2, the orientation of the printed layers with respect to the axis x_1 is given by the counterclockwise rotation $\alpha = 180° - \theta$, see again Fig. 1. This will be extensively used in the numerical simulations.

The stress-strain law in the global reference system reads $\boldsymbol{\varepsilon} = \mathbf{S}_0\boldsymbol{\sigma}$, being $\boldsymbol{\sigma} = [\sigma_{11} \quad \sigma_{22} \quad \sqrt{2}\sigma_{12}]$ and by $\boldsymbol{\varepsilon} = [\varepsilon_{11} \quad \varepsilon_{22} \quad \sqrt{2}\varepsilon_{12}]$ the stress and strain components, respectively, as written in Ox_1x_2. The compliance matrix reads:

$$\mathbf{S}_0 = \mathbf{R}(\alpha)\,\widehat{\mathbf{S}}_0\,\mathbf{R}^T(\alpha), \tag{2}$$

where the rotation matrix reads:

$$\mathbf{R}(\alpha) = \begin{bmatrix} c^2 & s^2 & \sqrt{2}cs \\ s^2 & c^2 & -\sqrt{2}cs \\ -\sqrt{2}cs & \sqrt{2}cs & c^2 - s^2 \end{bmatrix}, \tag{3}$$

where $c = \cos\theta = -\cos\alpha$ and $s = \sin\theta = \sin\alpha$ for brevity, see, e.g., [34, 35].

In the numerical simulations, results obtained for WAAM-produced stainless steel will be compared to those achieved using conventional grade 304L stainless steel. Young's modulus and Poisson's ratio of this latter read $E_s = 200$ GPa and $\nu_s = 0.3$, respectively [36].

Concerning WAAM-produced stainless steel, the minimum value of the apparent Young's modulus is found along the transversal direction, i.e., $E_{\min} = 106.09$ GPa, whereas the maximum one $E_{\max} = 246.82$ GPa is found for $\pm41.5°$. $E_{\min} < E_s$, but $E_{\max} > E_s$. The minimum value of the apparent shear modulus $G_{\min} = 42.14$ GPa arises when the axes are rotated by $\pm45°$ with respect to the material reference system, whereas the maximum value $G_{\max} = 151.25$ GPa is found when the axes are in the longitudinal and transversal directions. Due to the anisotropic behavior of the printed alloy, it must also be taken into account that any normal stress exerted along one of the symmetry axes of the medium induces axial strains only; when arbitrary directions are considered, both axial and shear strains arise.

Figure 2 provides polar plots of Young's modulus of the WAAM-produced stainless steel for different values of the printing orientation, i.e., $\alpha = 0°, 90°$ (a)
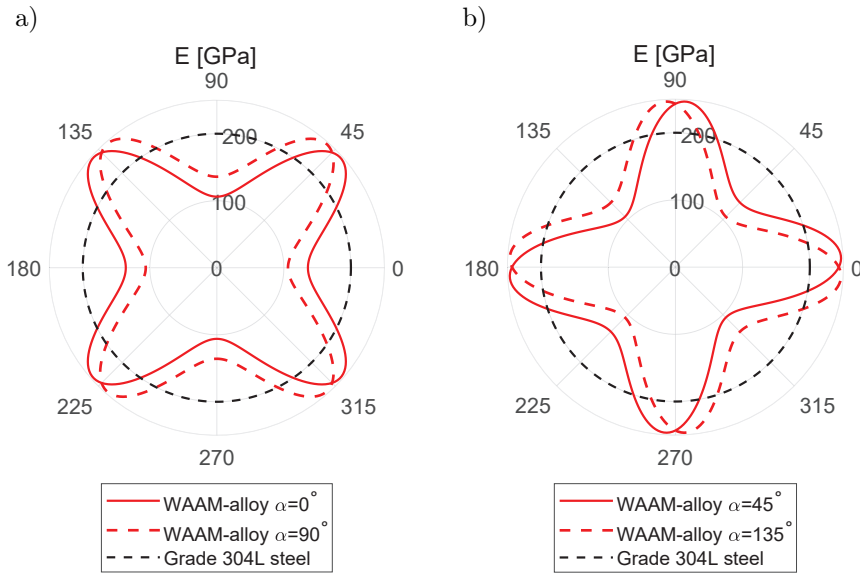
Fig. 2. Polar plot of Young's modulus of WAAM-produced stainless steel, for different values of the printing direction: a) $\alpha = 0°$ and $\alpha = 90°$, b) $\alpha = 45°$ and $\alpha = 135°$. In each plot, the angular coordinate provides the direction along which the modulus is given with respect to x_1. The value for grade 304 stainless steel is given for comparison.

and $\alpha = 45°, 135°$ (b). In each diagram, the angular coordinate identifies the direction along which the apparent value of the elastic modulus is given with respect to x_1. The elastic modulus of the conventional grade 304L stainless steel is reported for comparison.

For the specific case of I-beams, the typical structural engineering use foresees the application of gravity load acting on the same plane as the web, thus perpendicular to the flanges. Given that the flanges are subjected to in-plane axial loading (tension for the lower flange, compression for the upper flange), the optimal printing orientation for these two parts is set for $\alpha = 45°$, for which maximum stiffness is expected. On the other hand, given that the web is subjected to bending and shear loading, different printing orientations will be selected. In particular, the four principal printing orientations (e.g., at $\alpha = 0°$, $\alpha = 90°$, $\alpha = 45°$ and $\alpha = 135°$) will be considered.

3. Design of I-beam for minimum volume under deflection constraint

The design of I-beams for WAAM is herein formulated as a deflection-constrained minimum volume problem, which allows investigating optimal layouts

by enforcing requirements at the serviceability limit state. The numerical investigation presented in Sec. 4 includes simulations performed for different sets of prescribed printing orientations. Indeed, the amount of material needed to meet the deflection requirement is an outcome of the problem. This is used to provide comparisons when different assumptions are made concerning the adopted material and its printing orientation for the same example. As discussed in Sec. 3, the handling of the displacement-constrained optimization requires the solution of an adjoint problem to compute sensitivity. This is not the case with a compliance-constrained optimization, which is computationally cheaper. Being in compliance with the work of external loads at equilibrium, a minimum volume displacement-constrained formulation is equivalent to a compliance-constrained one when a single force is applied. Hence, the latter should be considered for such load if the computational cost is an issue. However, when distributed loads are dealt with, local control of the deflection calls for the adoption of a multiple set of displacement constraints. Dealing with the preliminary design of I-beams at the serviceability limit state under general load conditions, a displacement-constrained minimum volume formulation has been preferred.

A simplified modeling strategy is adopted to deal with the I-type cross-section of the herein considered beams: a regular mesh of four-node displacement-based elements is used for the web plate, whereas truss elements are adopted to cope with the flanges. The two sets of finite elements share the top and bottom nodes of the plane discretization. In the i-th of the n_w plane elements of the mesh, $0 \leq \rho_i \leq 1$ is a variable that controls the "density" of the orthotropic material, whereas $0 \leq A_j \leq A_{\max}$ is a variable that scales the area of the flanges in the j-th of the n_f trusses.

The solid isotropic material with penalization (SIMP) extensively used in TO is modified to handle orthotropic media as follows, see also [37–39]. The parameter α, see Subsec. 2.1, governs the orientation of the printed alloy. Working within a displacement-based finite element formulation, the direct form of the constitutive law is used, i.e., $\boldsymbol{\sigma} = \mathbf{C}\,\boldsymbol{\varepsilon}$. In the i-th element, the constitutive matrix $\mathbf{C}(\rho_i, \alpha)$ may be written as:

$$\mathbf{C}(\rho_i, \alpha) = \rho_i^p\ \mathbf{R}^T(\alpha)\,\widehat{\mathbf{C}}_0\,\mathbf{R}(\alpha) + \mathbf{C}_{\min}, \tag{4}$$

where $\widehat{\mathbf{C}}_0 = \widehat{\mathbf{S}}_0^{-1}$ is the stiffness matrix of the stress-strain relation of the WAAM material in the material reference system, see Eq. (1), $\mathbf{C}_{\min}$ prevents singularity in the "void" regions, and p is an interpolation parameter that penalizes intermediate densities. In the numerical simulations, p is increased from 3 to 6 during the optimization, see the continuation approach implemented e.g., in [40].

A problem for the design of the optimal topology of a WAAM-produced I-beam is stated as:

$$
\begin{cases}
\displaystyle \min_{0 \le \rho_i \le 1, 0 \le A_j \le A_{\max}} \mathcal{W} = \sum_{i=1}^{n_w} \rho_i\, W_{0,i} + \sum_{j=1}^{n_f} A_j\, l_j, \\[4mm]
\text{s.t.} \quad \mathbf{K}(\boldsymbol{\rho}, \alpha, \mathbf{A})\, \mathbf{U} = \left(\sum_{i=1}^{n_w} \rho_i^p\, \mathbf{K}_{0,i}^w(\alpha) + \sum_{j=1}^{n_f} A_j\, \mathbf{K}_{0,j}^f \right) \mathbf{U} = \mathbf{F}, \\[4mm]
u_k \le u_{\lim,k} \quad \text{for} \quad k = 1, ..., m.
\end{cases} \tag{5}
$$

In the above statement, the objective function is the weight of the structural element, which is computed through the sum of the contributions of the four-node elements in the web, $\rho_i\, W_{0,i}$, and of the two-node elements in the flanges, $A_j\, l_j$, being $W_{0,i}$ the volume of the i-th plane element for $\rho_i = 1$, and l_j the length of the j-th truss element.

Equation $(5)_2$ prescribes the discrete equilibrium of the structural element. The global stiffness matrix $\mathbf{K}(\boldsymbol{\rho}, \alpha, \mathbf{A})$ is computed by assembling the element contributions of the plane elements and the truss ones. The former ones can be conveniently written as $\rho_i^p\, \mathbf{K}_{0,i}^w(\alpha)$, where $\mathbf{K}_{0,i}^w(\alpha)$ refers to $\rho_i = 1$. The latter ones read $A_j\, \mathbf{K}_{0,j}^f$, where $\mathbf{K}_{0,j}^f$ refers to the unitary area of the j-th portion of the flange. The load vector $\mathbf{F}$ allows computing the nodal displacement vector $\mathbf{U}$ under the effect of any prescribed force. Design-independent loads are accounted for in the numerical investigations that follow.

The scalar quantity u_k stands for the k-th displacement component to be restrained. It may be written as:

$$
u_k = \mathbf{L}_k^T \mathbf{U}, \tag{6}
$$

where $\mathbf{L}_k$ is a vector made of zeros except for the entry referring to the displacement degree of freedom to be controlled, which takes a unitary value. Equation $(5)_3$ enforces a prescribed limit $u_{\lim,k}$ for each one of the m displacement components to be controlled.

The layouts achieved by means of the proposed numerical tool should be printed in sequential pieces (top flange, bottom flange and web plate) which are subsequently welded together. When either overhang issues affect any of the plates or a plate exceeds the maximum size allowed by the printer, slicing techniques are employed to divide the part into smaller pieces to be separately manufactured. These are subsequently welded to assemble the whole structural component. To give an example, a so-called "bridge" (i.e., the portion of a plate that horizontally links two raised points) is first printed using the base plate as a continuous support for the manufacturing process and then assembled at the right height by welding with surrounding pieces (the two raised points). Also, six-axis robots will further allow to overcome some of the overhang issues, by rotating

the base plate and printing at different angles. No control of the overhang is enforced in the simple optimization procedure implemented in the numerical simulations that follow. However, the proposed optimization procedure can be endowed with suitable methods available in the literature to control overhang angles within a TO framework, see Sec. 1.

3.1. Numerical implementation

A linear filter [41, 42] is implemented on the element variables ρ_i to prevent numerical issues that are well-known in TO, i.e., the arising of mesh dependence and checkerboard patterns [18]. The original variables ρ_i are mapped to the new set of filtered variables $\tilde{\rho}_i$ as follows:

$$\widetilde{\rho}_i = \frac{1}{\sum_{n_w} H_{ie}} \sum_{n_w} H_{ie}\, \rho_e,$$

$$H_{ie} = \max(0, r_{\min} - \text{dist}(i, e)), \tag{7}$$

where $\text{dist}(i, e)$ is the distance between the centroid of the i-th and e-th element, and $r_{\min}$ is the filter radius. Hence, the filtered densities are mapped to the set of projected (physical) densities $\widehat{\rho}_i$ in order to achieve crisp black/white solutions:

$$\widehat{\rho}_i = \frac{\tanh(\beta\eta) + \tanh(\beta(\widetilde{\rho}_i - \eta))}{\tanh(\beta\eta) + \tanh(\beta(1 - \eta))}, \tag{8}$$

with $\eta = [0, 1]$ and $\beta = [1, \infty]$, see in particular the formulation proposed in [43]. In the numerical section, $\eta = 0.5$, whereas β is smoothly increased during the simulations from 2 to 16 by adopting the same continuation approach implemented in [40]. Optimal layouts of web plates are given in terms of maps of $\widehat{\rho}_i$, or using the contour line $\widehat{\rho} = 0.5$.

The optimization problem in Eq. (5) is solved by means of mathematical programming, resorting to the method of moving asymptotes (MMA) [31]. The MMA minimizer is an iterative method. At each iteration, it provides the updated set of optimization unknowns, i.e., the current values of the densities ρ_i in the web and the values of the areas A_j in the flanges. A structured mesh using square finite elements is used to speed up the numerical tests. Indeed, $\mathbf{K}^w_{0,i}(\alpha)$ and $\mathbf{K}^f_{0,j}$ are computed only for one plane and one truss element at each iteration, respectively.

The adjoint method is used to compute sensitivity, see, e.g., [18]. Accordingly, u_k in Eq. (6) does not change whether a zero function derived from the equilibrium of Eq. (5)$_2$ is added at the right hand side, i.e.:

$$-\boldsymbol{\lambda}^T \left(\left(\sum_{i=1}^{n_w} \rho_i^p \, \mathbf{K}_{0,i}^w(\alpha) + \sum_{j=1}^{n_f} A_j \, \mathbf{K}_{0,j}^f \right) \mathbf{U} - \mathbf{F} \right), \tag{9}$$

where $\boldsymbol{\lambda}_k$ is any arbitrary but fixed vector. After re-arrangement of terms, the derivative of u_k with respect to the r-th unknown ρ_r and that with respect to the s-th unknown A_s may be computed respectively as:

$$\begin{aligned}
\frac{\partial u_k}{\partial \rho_r} &= -\boldsymbol{\lambda}_k^T \frac{\partial \mathbf{K}(\boldsymbol{\rho}, \alpha, \mathbf{A})}{\partial \rho_r} \mathbf{U}, \\
\frac{\partial u_k}{\partial A_s} &= -\boldsymbol{\lambda}_k^T \frac{\partial \mathbf{K}(\boldsymbol{\rho}, \alpha, \mathbf{A})}{\partial A_s} \mathbf{U},
\end{aligned} \tag{10}$$

where $\boldsymbol{\lambda}_k$ satisfies the adjoint equation:

$$\mathbf{K}(\boldsymbol{\rho}, \alpha, \mathbf{A}) \boldsymbol{\lambda}_k = \left(\frac{\partial u_k}{\partial \mathbf{U}} \right)^T = \mathbf{L}_k. \tag{11}$$

Equation $(10)_1$ is evaluated recalling that the derivative of the i-th four-node element stiffness matrix with respect to ρ_r is equal to $p\rho_i^{p-1} \mathbf{K}_{0,i}^w(\alpha)$. This sensitivity is null if $i \neq r$. Concerning Eq. $(10)_2$, the derivative of the j-th two-node element stiffness matrix with respect to A_s is equal to $\mathbf{K}_{0,j}^f$ for $j = s$, otherwise it equals zero.

The derivatives with respect to the filtered variables $\widetilde{\rho}_i$ and the projected ones $\widehat{\rho}_i$ can be easily computed by applying the chain rule to Eqs. (7) and (8), respectively. It is also observed that at each iteration of the minimization procedure only $m + 1$ linear systems are solved to evaluate the constraints and their sensitivities, i.e., Eqs. $(5)_2$ and (11), the latter for $k = 1, ..., m$. Both linear systems share the same stiffness matrix.

4. Numerical simulations

In this section numerical simulations considering the optimal design of I-beams are presented. Geometry and displacement boundary conditions for the examples addressed in this work are given in Fig. 3. In particular, two types of configurations are studied: cantilever beams and simply-supported beams. For both of them, two different slenderness ratios are considered, namely $3L \times L$ and $6L \times L$. The same thickness is assumed for both the web and the flanges. The maximum width of the flanges, which governs $A_{\max}$ in the side constraint of the variables A_j, is one half of the height of the web, i.e., $L/2$. The filter radius $r_{\min}$ is $L/12$.

Optimal layouts are sought considering at first isotropic stainless steel and then a selection of printing orientations for the WAAM-produced alloy. In the latter case, it is assumed that the elastic modulus of the flange trusses is E_D,

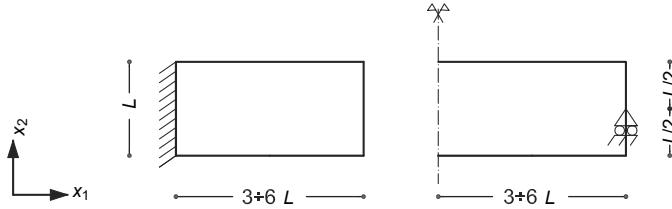Fig. 3. Geometry and displacement boundary conditions for the examples addressed in the numerical simulations.

i.e., that flanges are printed with a 45°-inclined build orientation with respect to their longitudinal axis.

In all the examples, the deflection constraints enforce that the vertical displacement at each one of the loaded points is less than 1.50 times the value found in case of an I-beam entirely made of Grade 304L isotropic stainless steel ($\rho_i = 1$ all over the web and $A_j = A_{\max}$ throughout the flanges). It is found that all the layouts achieved for the same example undergo the same maximum displacement, i.e., they exhibit equal stiffness. The results presented next are compared in terms of volume fraction of the material at convergence V_f, which is the ratio of the last value of the objective function $\mathcal{W}$ to the weight of a "full material" I-beam.

In Tables 1 and 2, data summaries of the numerical applications concerning cantilever beams and simply-supported I-beams of Subsecs. 4.1 and 4.2 are reported, respectively.

TABLE 1. Data summary for the numerical applications concerning cantilever beams in Subsec. 4.1.

Figure	Beam type	Load type	Material	Volume fraction [%]
4a			Grade 304L steel	48.3
4b	$3L \times L$ cantilever beam	point force	WAAM alloy, $\alpha = 0°$	75.0
4c			WAAM alloy, $\alpha = 45°$	48.4
4d			WAAM alloy, $\alpha = 135°$	49.8
5			Grade 304L steel	56.4
6a			WAAM alloy, $\alpha = 0°$	44.8
6b	$3L \times L$ cantilever I-beam	point force	WAAM alloy, $\alpha = 90°$	44.1
6c			WAAM alloy, $\alpha = 45°$	55.2
6d			WAAM alloy, $\alpha = 135°$	57.3
7a			Grade 304L steel	52.0
7b			WAAM alloy, $\alpha = 0°$	38.4
7c	$6L \times L$ cantilever I-beam	point force	WAAM alloy, $\alpha = 90°$	38.4
7d			WAAM alloy, $\alpha = 45°$	45.4
7e			WAAM alloy, $\alpha = 135°$	45.8

TABLE 2. Data summary for the numerical applications concerning simply-supported I-beams in Subsec. 4.2.

Figure	Beam type	Load type	Material	Volume fraction [%]
8a	$3L \times L$ simply-supported I-beam	point force	Grade 304L steel	55.4
8b			WAAM alloy, $\alpha = 90°$	43.2
8c			WAAM alloy, $\alpha = 135°$	54.9
9a	$6L \times L$ simply-supported I-beam	point force	Grade 304L steel	52.2
9b			WAAM alloy, $\alpha = 90°$	38.4
9c			WAAM alloy, $\alpha = 135°$	45.3
9a	$6L \times L$ simply-supported I-beam	distributed load	Grade 304L steel	52.2
9b			WAAM alloy, $\alpha = 90°$	40.7
9c			WAAM alloy, $\alpha = 135°$	43.7

4.1. Cantilever beams

A set of numerical simulations is presented, concerning a $3L \times L$ cantilever beam, see Fig. 3. The specimen is acted upon by a vertical force located at the top right corner of the rectangular domain. A mesh of 300×100 four-node elements is adopted for the web, along with 2×300 two-node elements for the flanges, if any.

At first, numerical simulations are devoted to estimate the effect of the WAAM stainless steel anisotropy on the optimal design, investigating the web plate without flanges. The achieved results are given in Fig. 4. The optimal design achieved in the case of conventional isotropic stainless steel is taken as a reference, see Fig. 4a with $V_f = 48.3\%$. The density maps concerning WAAM stainless steel are endowed with a sketch that stands for the relevant printing direction: lines denote the build orientation of the printed layers, i.e., the longitudinal direction of the material with respect to the axes of the design domain
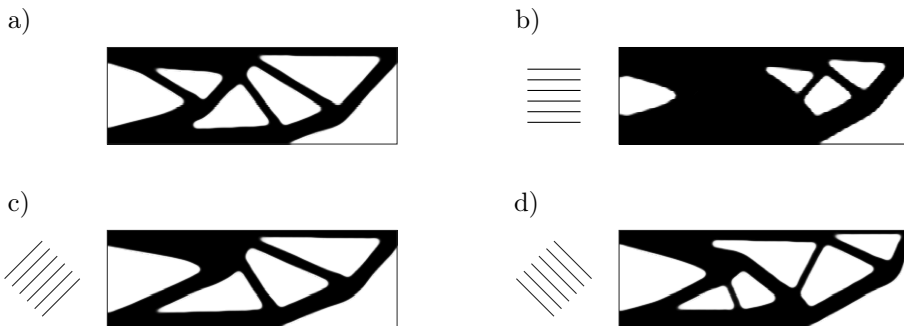

FIG. 4. $3L \times L$ cantilever beam without flanges – optimal design with a) isotropic material $V_f = 48.3\%$, and WAAM material for prescribed printing orientation: b) $\alpha = 0°$ $V_f = 75.0\%$, c) $\alpha = 45°$ $V_f = 48.4\%$, d) $\alpha = 135°$ $V_f = 49.8\%$. No feasible solution found for $\alpha = 90°$.

(see Fig. 1). It is remarked that, in order to get high quality printed parts, the printing direction is normally kept horizontal during the WAAM fabrication process, whereas the part is oriented. Nonetheless, for easy comparisons among different layouts, the axes of the design domain are given the same orientation in all the pictures commented in this section, while the build orientation is oriented accordingly. In Fig. 4b, the optimal design for $\alpha = 0°$ is presented. The apparent elastic modulus of the WAAM alloy in the longitudinal direction, E_L, is nearly 30% lower than the elastic modulus for conventional stainless steel E_S, see also Fig. 2a. Indeed, the volume fraction for $\alpha = 0°$ is much higher than in the reference case. No feasible solution can be found for $\alpha = 90°$, due to the fact that E_T is even less than E_L. When exploring the material orientations $\alpha = 45°$ and $\alpha = 135°$, the volume fraction is not far from that found for grade 304L stainless steel, as well as the optimal layouts. Both layouts take full advantage of the fact that the apparent elastic modulus along x_1 is almost equal to $E_{\max}$. Minor differences arise when comparing the layouts in Figs. 4c and 4d. This is due to the fact that the polar diagrams in Fig. 2b do not completely overlap, because $E_L \neq E_T$.

Figures 5 and 6 concern the optimal design of a web plate with flanges, i.e., the I-beam. The layout achieved in the case of conventional stainless steel is given in the former figure, where a density map for the web plate and a three-
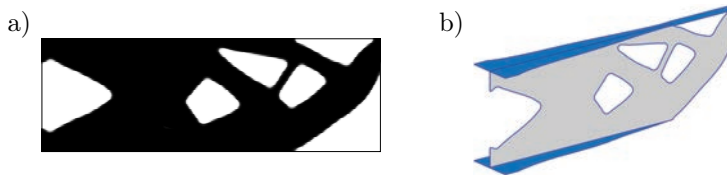

FIG. 5. $3L \times L$ cantilever I-beam – optimal design with isotropic material $V_f = 56.4\%$: a) density map for the web plate and b) three-dimensional view of the structural component.
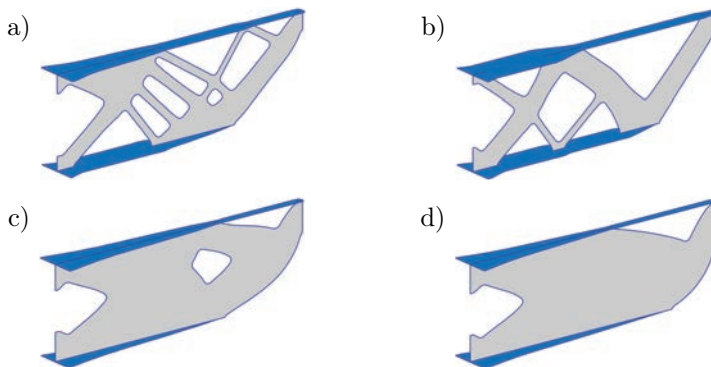

FIG. 6. $3L \times L$ cantilever I-beam – optimal design with WAAM material for prescribed printing orientation: a) $\alpha = 0°$ $V_f = 44.8\%$, b) $\alpha = 90°$ $V_f = 44.1\%$, c) $\alpha = 45°$ $V_f = 55.2\%$, d) $\alpha = 135°$ $V_f = 57.3\%$.

dimensional view of the structural component are given. The volume fraction of this reference design reads $V_f = 56.4\%$. As expected, the width of the flanges increases approaching the clamped side, as the bending moment of the cantilever increases. However, a strut-and-tie model arises at the tip inducing a constant axial stress in a limited portion of the upper chord. Apart from the tip, the web plate has a big cavity next to the support, where the shear action is conveyed both at the top and the bottom region of the cross-section.

Figure 6 addresses optimal I-beams designed for WAAM. With respect to the previous solution, the flanges benefit from the increased elastic modulus $(E_D > E_S)$, whereas the printing orientation remarkably affects the topology of the web. The optimal layouts achieved for the material orientations $\alpha = 0°$ and $\alpha = 90°$, see Figs. 6a and 6b, respectively, take full advantage of the fact that the apparent elastic modulus along the directions inclined of approximately 45° and 135° with respect to the axes of the design domain is not far from $E_{\max}$. In spite of the different topology of the overall layouts, both design are approximately 20% lighter than the reference solution. The optimal layouts achieved using $\alpha = 45°$ and $\alpha = 135°$ are variations of the isotropic solution, more or less with the same volume fraction.

An additional set of numerical simulations is performed on a longer $(6L \times L)$ cantilever beam, using the same boundary conditions. A mesh of 600×100 four-node elements is adopted for the web, whereas 2×600 two-node elements are used for the flanges. The optimal design for the case of isotropic material, which is represented in Fig. 7a, has a smooth variation of the width of the flanges and
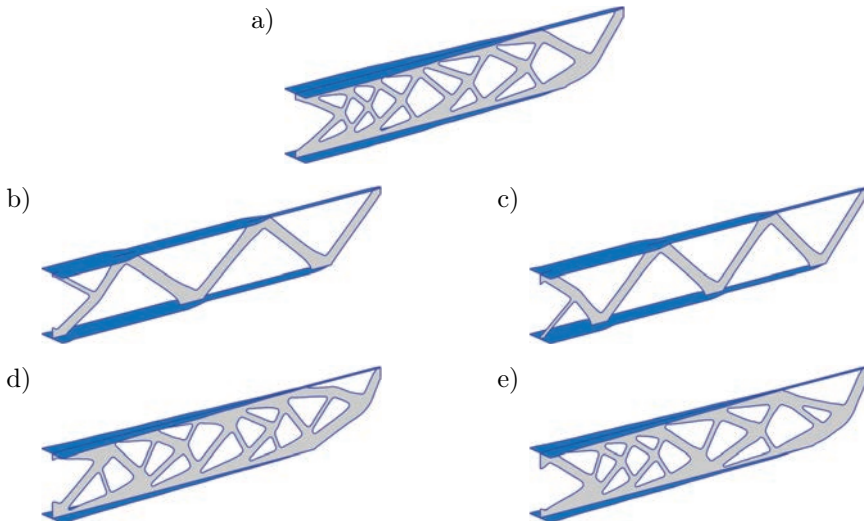

FIG. 7. $6L \times L$ cantilever I-beam – optimal design with isotropic material a) $V_f = 52.0\%$, and WAAM material for prescribed printing orientation: b) $\alpha = 0°$ $V_f = 38.4\%$, c) $\alpha = 90°$ $V_f = 38.4\%$, d) $\alpha = 45°$ $V_f = 45.4\%$, and e) $\alpha = 135°$ $V_f = 45.8\%$.

is characterized by a perforated web whose shape recalls Michell's solutions, see in particular [3]. The volume fraction reads $V_f = 52\%$. For $\alpha = 0°$ and $\alpha = 90°$, see Figs. 7b and 7c, respectively, a very effective truss-like solution arises. The width of the chords is piecewise constant, whereas web trusses are inclined by approximately $\pm 45°$ with respect to the axes of the design domain in order to exploit the maximum value of the apparent elastic modulus of the printed alloy. Both layouts are nearly 25% lighter than the reference one. Again, the optimal layouts achieved using $\alpha = 45°$ and $\alpha = 135°$ are variations of the isotropic layout. Indeed, the solutions represented in Figs. 7d and 7e mainly differ in the orientation of several members of the web, see also Fig. 2b. Due to the increased slenderness of the cantilever, the enhanced elastic modulus of the flanges allows achieving lighter solutions with respect to the design in Fig. 7a.

4.2. Simply-supported beam

A $3L \times L$ simply-supported beam is addressed, see Fig. 3. The specimen is acted upon by a vertical force that is located at midspan, along the top side of the rectangular domain. It is assumed that the web plate is printed using two mirrored orientations with respect to the vertical axis of the rectangular domain. Hence, due to symmetry in the geometry, boundary conditions and material orientation, only half of the specimen is analyzed and represented in the figures that follow.

The optimal simply-supported I-beam derived using conventional stainless steel is depicted in Fig. 8a, with a volume fraction $V_f = 55.4\%$. As found for the short cantilever of the previous section, the width of the flanges gradually changes depending on the trend of the bending moment, whereas a massive web plate appears to withstand the shear force. Figure 8b shows the lighter truss-like design that can be achieved for $\alpha = 90°$: the weight saving is about 22%.
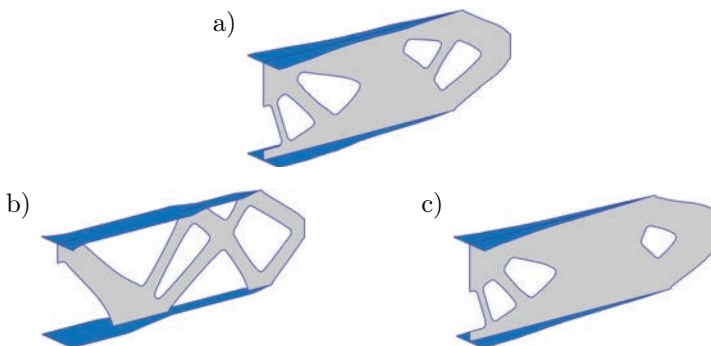

FIG. 8. Simply-supported I-beam – optimal design with a) isotropic material $V_f = 55.4\%$, and WAAM material for prescribed printing orientation: b) $\alpha = 90°$ $V_f = 43.2\%$ and c) $\alpha = 135°$ $V_f = 54.9\%$.

In Fig. 8c the optimal solution found in the case of $\alpha = 135°$ has a similar layout to that of the isotropic structure, as well as the volume fraction. Similar results can be derived for $\alpha = 0°$ and $\alpha = 45°$.

A further set of numerical simulations is performed considering a longer $6L \times L$ simply-supported beam, while adopting the same boundary conditions. The comments already given about the slender cantilever in Fig. 7 apply. The most efficient solution is that for $\alpha = 90°$, see Fig. 9b, with a weight saving of about 25% with respect to the one achieved for isotropic steel, see Fig. 9a. The width of the flanges is piecewise constant. The web design next to the lateral support is similar to that seen in the shorter simply-supported beam, whereas $\pm 45°$-inclined members take full advantage of the maximum apparent elastic modulus provided by the material in the remaining part of the shear resisting plate. The optimal solution found for $\alpha = 135°$, see Fig. 9c, in more similar to the design for isotropic material, but with a weight that is approximately 13% less.
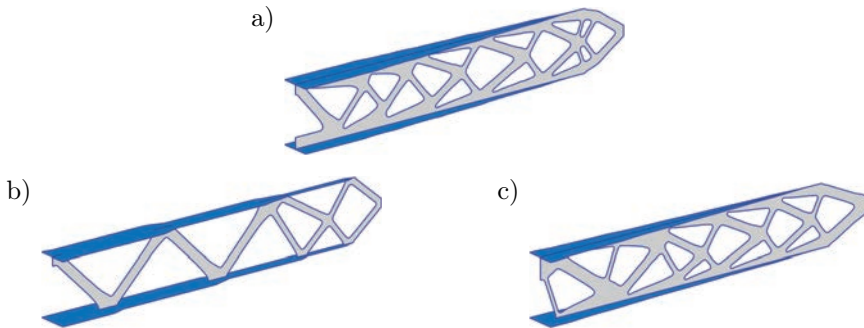

FIG. 9. Slender simply-supported I-beam – optimal design with a) isotropic material $V_f = 52.2\%$, and WAAM material for prescribed printing orientation: b) $\alpha = 90°$ $V_f = 38.4\%$ and c) $\alpha = 135°$ $V_f = 45.3\%$.

Given that the applied load remarkably affects the optimal layout, additional studies are made with a different loading configuration. In particular, in Fig. 10, optimal layouts are given considering a distributed load acting along the upper side of the slender simply-supported beam (excluding a portion of length $L/2$ next to the lateral support). Instead of being constant throughout the half of the beam, the shear force diagram increases from zero at midspan to its maximum value at the lateral support. For this reason, especially the optimal design found in the case of isotropic material, see Fig. 10a, and that for WAAM alloy with printing direction $\alpha = 135°$, see Fig. 10c, have large holes in the web plates at midspan. Again, the most efficient solution is found for $\alpha = 90°$, see Fig. 10b, with a weight saving of more than 20% with respect to the one achieved for conventional stainless steel. A main cross-shaped layout provides shear resistance
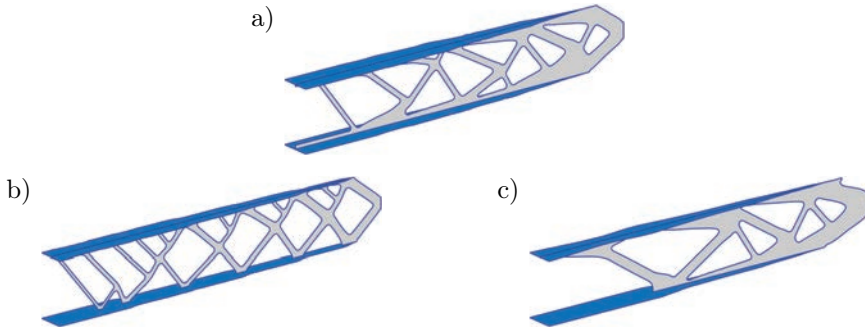
Fig. 10. Slender simply-supported I-beam with distributed load – optimal design with a) isotropic material $V_f = 52.2\%$, and WAAM material for prescribed printing orientation: b) $\alpha = 90°$ $V_f = 40.7\%$ and c) $\alpha = 135°$ $V_f = 43.7\%$.

in the web plate, whereas minor 135°-inclined members exploits the maximum apparent elastic modulus provided by the printed material to give support to the distributed load acting on the top of the beam.

5. Conclusions and ongoing research

Wire-and-arc additively manufactured (WAAM) stainless steel plates resulted to be significantly affected by their relative printing direction. In particular, experimental studies revealed an orthotropic behavior that caused a remarkable difference in terms of apparent elastic modulus depeding on the relative printing orientation of the specimen tested. For this reason, the first numerical investigations were performed to adopt TO for the orthotropic material, highlighting that the optimal design of single-plate WAAM specimens were severely affected by their printing direction.

In this contribution, the optimal design of WAAM-produced I-beams was addressed assuming that a web plate and two flat flanges are printed and subsequently welded to assemble the structural component. A formulation of displacement-constrained TO was implemented to design minimum weight specimens resorting to a simplified two-dimensional model of the I-beam. Numerical simulations were performed, with the aim of comparing the shape and the weight of specimens designed to meet the same requirement at the serviceability limit state, using (i) conventional isotropic (grade 304L) stainless steel and (ii) WAAM-produced orthotropic stainless steel at prescribed printing orientations. In the latter case, it is assumed that flanges are printed with a 45°-inclined build orientation with respect to the their longitudinal axis, thus exploiting an elastic modulus than is higher that that of the isotropic steel.

A remarkable variability in terms of weight and geometry of the optimal solutions is reported, depending on the prescribed orientation. Working with single-

plate WAAM specimens, it is found that printing directions that are inclined with respect to the beam axis perform better than the horizontal and vertical build directions. Indeed, the structural behavior is mainly governed by the axial strains due to bending. When moving to I-beams, the outcome is the opposite. Adopting horizontal or vertical build directions, effective truss-like designs arise. Indeed, piecewise constant flanges work in conjunction with web trusses that are aligned with the direction of maximum apparent elastic modulus of the printed material. Weight saving of up to 25% is registered with respect to the solution found for conventional stainless steel.

The proposed algorithm can be conveniently used to save weight in the WAAM process by investigating solutions for any load conditions and restraint configurations. Due to the simple optimization problem herein implemented, this must be intended as a preliminary design tool for I-beam design. The adoption of mathematical programming allows implementing other enforcements within the considered displacement-constrained formulation for orthotropic materials, such as overhang constraints, buckling constraints and stress constraints, see in particular [44]. Also, more complex modeling could be effectively considered to account for residual stresses. These aspects are crucial to design effective structural components and are currently under investigation with the aim of designing parts for structural applications and validating their response through experimental tests.

References

1. M. Carpo, *The digital turn in architecture 1992–2012*, John Wiley and Sons, 2013, doi: 10.1002/9781118795811.

2. S. Adriaenssens, P. Block, D. Veenendaal, C. Williams, *Shell structures for architecture: form finding and optimization*, Routledge, 2014, doi: 10.4324/9781315849270.

3. T. Lewiński, T. Sokół, C. Graczykowski, *Michell Structures*, Springer 2018, doi: 10.1007/978-3-319-95180-5.

4. M. Bruggi, A constrained force density method for the funicular analysis and design of arches, domes and vaults, *International Journal of Solids and Structures*, **193–194**: 251–269, 2020, doi: 10.1016/j.ijsolstr.2020.02.030.

5. C. Boje, A. Guerriero, S. Kubicki, Y. Rezgui, Towards a semantic Construction Digital Twin: Directions for future research, *Automation in Construction*, **114**: 103179, 2020, doi: 10.1016/j.autcon.2020.103179.

6. W.E. Frazier, Metal additive manufacturing: A review, *Journal of Materials Engineering and Performance*, **23**: 1917–1928, 2014, doi: 10.1007/s11665-014-0958-z.

7. B. Wu *et al.*, A review of the wire arc additive manufacturing of metals: properties, defects and quality improvement, *Journal of Manufacturing Processes*, **35**: 127–139, 2018, doi: 10.1016/j.jmapro.2018.08.001.

8. C. Buchanan, L. Gardner, Metal 3D printing in construction: A review of methods, research, applications, opportunities and challenges, *Engineering Structures*, **180**: 332–348, 2019, doi: 10.1016/j.engstruct.2018.11.045.

9. M. Dinovitzer, X. Chen, J. Laliberte, X. Huang, H. Frei, Effect of wire and arc additive manufacturing (WAAM) process parameters on bead geometry and microstructure, *Additive Manufacturing*, **26**: 138–146, 2019, doi: 10.1016/j.addma.2018.12.013.

10. L. Ji, J. Lu, C. Liu, C. Jing, H. Fan, S. Ma, Microstructure and mechanical properties of 304L steel fabricated by arc additive manufacturing, MATEC Web of Conferences, 2017, doi: 10.1051/matecconf/201712803006.

11. V. Laghi, M. Palermo, G. Gasparini, V.A. Girelli, T. Trombetti, Experimental results for structural design of Wire-and-Arc Additive Manufactured stainless steel members, *Journal of Constructional Steel Research*, **167**: 105858, 2020, doi: 10.1016/j.jcsr.2019.105858.

12. V. Laghi, M. Palermo, L. Tonelli, G. Gasparini, L. Ceschini, T. Trombetti, Tensile properties and microstructural features of 304L austenitic stainless steel produced by wire-and-arc additive manufacturing, *International Journal of Advanced Manufacturing Technology*, **106**(9–10): 3693–3705, 2020, doi: 10.1007/s00170-019-04868-8.

13. V. Laghi, M. Palermo, G. Gasparini, V.A. Girelli, T. Trombetti, On the influence of the geometrical irregularities in the mechanical response of wire-and-arc additively manufactured planar elements, *Journal of Constructional Steel Research*, **178**: 106490, 2021, doi: 10.1016/j.jcsr.2020.106490.

14. P. Kyvelou *et al.*, Mechanical and microstructural testing of wire and arc additively manufactured sheet material, *Materials and Design*, **192**: 108675, 2020, doi: 10.1016/j.matdes.2020.108675.

15. V. Laghi *et al.*, Experimentally-validated orthotropic elastic model for wire-and-arc additively manufactured stainless steel, *Additive Manufacturing*, **42**: 101999, 2021, doi: 10.1016/j.addma.2021.101999.

16. N. Hadjipantelis, B. Weber, C. Buchanan, L. Gardner, Description of anisotropic material response of wire and arc additively manufactured thin-walled stainless steel elements, *Thin-Walled Structures*, **171**: 108634, 2022, doi: 10.1016/j.tws.2021.108634.

17. W. Zhang, J. Zhu, T. Gao, *Topology Optimization in Engineering Structure Design*, Elsevier, 2016.

18. M.P. Bendsoe, O. Sigmund, *Topology Optimization: Theory, Methods and Applications*, Springer, 2003.

19. O. Sigmund, K. Maute, Topology optimization approaches: A comparative review, *Structural and Multidisciplinary Optimization*, **48**(6): 1031–1055, 2013, doi: 10.1007/s00158-013-0978-6.

20. J. Liu *et al.*, Current and future trends in topology optimization for additive manufacturing, *Structural and Multidisciplinary Optimization*, **57**(6): 2457–2483, 2018, doi: 10.1007/s00158-018-1994-3.

21. L. Meng *et al.*, From topology optimization design to additive manufacturing: Today's success and tomorrow's roadmap, *Archives of Computational Methods in Engineering*, **27**(2020): 805–830, 2019, doi: 10.1007/s11831-019-09331-1.

22. G. Allaire, B. Bogosel, Optimizing supports for additive manufacturing, *Structural and Multidisciplinary Optimization*, **58**(6): 2493–2515, 2018, doi: 10.1007/s00158-018-2125-x.

23. M. Bruggi, N. Parolini, F. Regazzoni, M. Verani, Topology optimization with a time-integral cost functional, *Finite Elements in Analysis and Design*, **140**: 11–22, 2018, doi: 10.1016/j.finel.2017.10.011.

24. G. Allaire, C. Dapogny, R. Estevez, A. Faure, G. Michailidis, Structural optimization under overhang constraints imposed by additive manufacturing technologies, *Journal of Computational Physics*, **351**: 295–328, 2017, doi: 10.1016/j.jcp.2017.09.041.

25. O. Amir, Y. Mass, Topology optimization for staged construction, *Structural and Multidisciplinary Optimization*, **57**(4): 1679–1694, 2018, doi: 10.1007/s00158-017-1837-7.

26. X. Guo, J. Zhou, W. Zhang, Z. Du, C. Liu, Y. Liu, Self-supporting structure design in additive manufacturing through explicit topology optimization, *Computer Methods in Applied Mechanics and Engineering*, **323**: 27–63, 2017, doi: /10.1016/j.cma.2017.05.003.

27. M. Langelaar, Combined optimization of part topology, support structure layout and build orientation for additive manufacturing, *Structural and Multidisciplinary Optimization*, **57**(5): 1985–2004, 2018, doi: 10.1007/s00158-017-1877-z.

28. W. Wang, D. Munro, C.C.L. Wang, F. van Keulen, J. Wu, Space-time topology optimization for additive manufacturing: Concurrent optimization of structural layout and fabrication sequence, *Structural and Multidisciplinary Optimization*, **61**: 1–18, 2020, doi: 10.1007/s00158-019-02420-6.

29. M. Bruggi, V. Laghi, T. Trombetti, Simultaneous design of the topology and the build orientation of Wire-and-Arc Additively Manufactured structural elements, *Computers and Structures*, **242**: 106370, 2021, doi: 10.1016/j.compstruc.2020.106370.

30. L.L. Stromberg, A. Beghini, W.F. Baker, G.H. Paulino, Topology optimization for braced frames: Combining continuum and beam/column elements, *Engineering Structures*, **37**: 106–124, 2012, doi: 10.1016/j.engstruct.2011.12.034.

31. K. Svanberg, Method of moving asymptotes – A new method for structural optimization, *International Journal for Numerical Methods in Engineering*, **24**(2): 359–373, 1987, doi: 10.1002/nme.1620240207.

32. S.W. Williams, F. Martina, A.C. Addison, J. Ding, G. Pardal, P. Colegrove, Wire + Arc additive manufacturing, *Materials Science and Technology*, **32**(7): 641–647, 2016, doi: 10.1179/1743284715Y.0000000073.

33. V. Laghi *et al.*, Mechanical response of dot-by-dot wire-and-arc additively manufactured 304L stainless steel bars under tensile loading, *Construction and Building Materials*, **318**: 125925, 2022, doi: 10.1016/j.conbuildmat.2021.125925.

34. M.M. Mehrabadi, S.C. Cowin, Eigentensors of linear anisotropic elastic materials, *Quarterly Journal of Mechanics and Applied Mathematics*, **43**: 15–41, 1990, doi: 10.1093/qjmam/43.1.15.

35. P. Vannucci, Anisotropic elasticity, [in:] *Lecture Notes in Applied and Computational Mechanics book series*, Vol. 85, Springer International Publishing, 2018, doi: 10.1007/978-981-10-5439-6.

36. European Committee for Standardization CEN (2015) EN 1993-1-4:2006+a1:2015 Eurocode 3 Design of Steel Structures, Part 1–4: General Rules Supplementary Rules for Stainless Steel.

37. M. Bruggi, A. Taliercio, Optimal strengthening of concrete plates with unidirectional fiber-reinforcing layers, *International Journal of Solids and Structures*, **67–68**: 311–325, 2015, doi: 10.1016/j.ijsolstr.2015.04.033.

38. D. Briccola, M. Bruggi, Analysis of 3D linear elastic masonry-like structures through the API of a finite element software, *Advances in Engineering Software*, 2019, **133**: 60–75, doi: 10.1016/j.advengsoft.2019.04.009.

39. M. Bruggi, A. Taliercio, Hierarchical infills for additive manufacturing through a multiscale approach, *Journal of Optimization Theory and Applications*, **187**(3): 654–682, 2020, doi: 10.1007/s10957-020-01685-y.

40. F. Ferrari, O. Sigmund, A new generation 99 line Matlab code for compliance topology optimization and its extension to 3D, *Structural and Multidisciplinary Optimization*, **62**(4): 2211–2228, 2020, doi: 10.1007/s00158-020-02629-w.

41. T. Borrvall, J. Petersson, Topology optimization using regularized intermediate density control, *Computer Methods in Applied Mechanics and Engineering*, **190**(37–38): 4911–4928, 2001, doi: 10.1016/S0045-7825(00)00356-X.

42. B. Bourdin, Filters in topology optimization, *International Journal for Numerical Methods in Engineering*, **50**(9): 2143–2158, 2001, doi: 10.1002/nme.116.

43. F. Wang, B. Lazarov, O. Sigmund, On projection methods, convergence and robust formulations in topology optimization, *Structural and Multidisciplinary Optimization*, **43**(6): 767–784, 2011, doi: 10.1007/s00158-010-0602-y.

44. B. Blachowski, P. Tauzowski, J. Logo, Yield limited optimal topology design of elastoplastic structures, *Structural and Multidisciplinary Optimization*, **61**(5): 1953–1976, 2020, doi: 10.1007/s00158-019-02447-9.